Spatial variation of the two-fold anisotropic superconducting gap in a monolayer of $FeSe_{0.5}Te_{0.5}$ on a topological insulator

A. Kamlapure,[1,*] S. Manna,[1] L. Cornils,[1] T. Hänke,[1] M. Bremholm,[2] Ph. Hofmann,[3] J. Wiebe,[1,†] and R. Wiesendanger[1]

[1]*Department of Physics, University of Hamburg, Jungiusstrasse 11, D-20355 Hamburg, Germany*

[2]*Department of Chemistry and Center for Materials Crystallography, Aarhus University, Denmark*

[3]*Department of Physics and Astronomy, and Interdisciplinary Nanoscience Center iNANO, Aarhus University, Denmark*

(Received 12 September 2016; revised manuscript received 7 February 2017; published 13 March 2017)

We present a low temperature scanning tunneling spectroscopy (STS) study of the superconducting properties of monolayers of $FeSe_{0.5}Te_{0.5}$ grown on the three-dimensional (3D) topological insulator $Bi_2Se_{1.2}Te_{1.8}$. While the morphology and the overall transition temperature resembles those of similarly doped bulk crystals, we find a two-fold anisotropic s-wave gap function. The two-fold nature of the gap symmetry is evident from the Bogoliubov quasiparticle interference (QPI) pattern, which shows distinct C_2 symmetric scattering intensities. Spatially resolved spectroscopic data shows a strong inhomogeneity in the size and anisotropy strength of the energy gaps, which cannot be correlated merely to the local chemical disorder. Instead, we argue that the gap inhomogeneity emerges with a similar mechanism as in disordered superconductors. Our sample system provides an ideal platform to study unconventional superconductivity in close proximity to a topological insulator.

DOI: 10.1103/PhysRevB.95.104509

I. INTRODUCTION

The discovery of Fe-based superconductors (FeSCs) is an important hallmark in the field of superconductivity [1]. It provides the potential route to understanding the microscopic mechanism of unconventional superconductivity in high T_c cuprates because of the analogous phase diagram of both materials featuring an antiferromagnetically ordered parent compound. The electronic structure of FeSC is fairly complex with both electron and hole multibands. In these intrinsically multiorbital systems, both spin fluctuations [2] and orbital fluctuations [3] have been argued to be responsible for the origin of superconductivity. However, recent investigations have shown that strong spin-orbit coupling lifts degeneracies between different d bands and is intimately linked to the observed electronic anisotropy and nematicity [4,5]. As far as the stoichiometry is concerned, the Fe chalcogenides (FeCh), $Fe_{1+\delta}Se_xTe_{1-x}$, are the simplest systems of the different families of FeSC with optimal $T_c \sim 15.2\,\mathrm{K}$ around $x = 0.5$ [6]. Regardless of the simple structure, the electronic and magnetic properties of FeCh are extremely sensitive to the growth conditions and pressures [7–11]. Particularly in thin films, T_c strongly depends on the substrates and is argued to be dependent on the ratio of the lattice parameters (c/a) [8,9]. Moreover, FeCh have recently gained interest due to the observation of record high T_c values in for monolayers (MLs) of FeCh on $SrTiO_3$ substrates [12,13].

Concerning the order parameter (OP) for the FeCh systems, numerous works suggest $s \pm$ pairing with nodeless superconductivity for bulk $FeSe_{0.5}Te_{0.5}$ [14,15]. However, there is a dispute about the $s \pm$ picture [16,17], which makes the exact structure of the OP unclear. On the other hand, the V-shaped superconducting gap observed in FeSe supports nodal superconductivity [18]. Moreover, there were recent results on the nematic behavior in bulk FeCh [19,20], which is argued to be resulting from the lifting of orbital degeneracy, supporting $s++$ pairing [3,21]. Concerning the anisotropy of the gap of FeCh, both two-fold [18,22] and four-fold symmetries [23,24] have been found. All these findings on bulk and thin films of FeCh show that the OP crucially depends on the film thickness, doping, and substrates.

In this paper, we explore the superconducting properties of a ML of $FeSe_{0.5}Te_{0.5}$ grown on the topological insulator $Bi_2Se_{1.2}Te_{1.8}$ by high-resolution scanning tunneling spectroscopy (STS). We observe inhomogeneous superconductivity along with a distinct C_2 symmetry in spectral images. Interestingly, both the gap size and its two-fold anisotropy markedly vary on the length scale of 10–15 nm, which is much larger than the length scale of chemical disorder. We propose a similar mechanism of gap inhomogeneity, as observed for high-T_c cuprates and strongly disordered conventional superconductors. It is important to note that an angle-resolved photoemission spectroscopy (ARPES) study of the FeSe thin film system similar to ours has proven that the topological surface state in the substrate below the chalcogenide layer is preserved [25]. Therefore, our sample system represents an s-wave SC in close proximity to a topological surface state. Thereby, it provides an ideal platform to study the theoretically predicted topological superconductivity and to explore the expected Majorana physics [26,27].

II. EXPERIMENTAL DETAILS

The MLs of $FeSe_xTe_{1-x}$ were grown by evaporating nominally 0.5 ML of Fe on the topological insulator $Bi_2Se_{1.2}Te_{1.8}$ [28] at room temperature under ultrahigh vacuum conditions and subsequently annealing the sample at 300 °C for about 15 minutes. The superconducting properties of the sample were then investigated *in situ* by measuring spatially resolved differential tunneling conductance spectra as a function of sample voltage V (dI/dV) with bulk Cr tip using lock-in technique after stabilization with typical currents of $I_{\mathrm{stab}} = 400\,\mathrm{pA}$, voltages of $V_{\mathrm{stab}} = 10\,\mathrm{mV}$, and modulation voltages of $V_{\mathrm{mod}} = 100\,\mu\mathrm{V}$ ($f = 827\,\mathrm{Hz}$) [29].

*akamlapu@physnet.uni-hamburg.de

†jwiebe@physnet.uni-hamburg.de

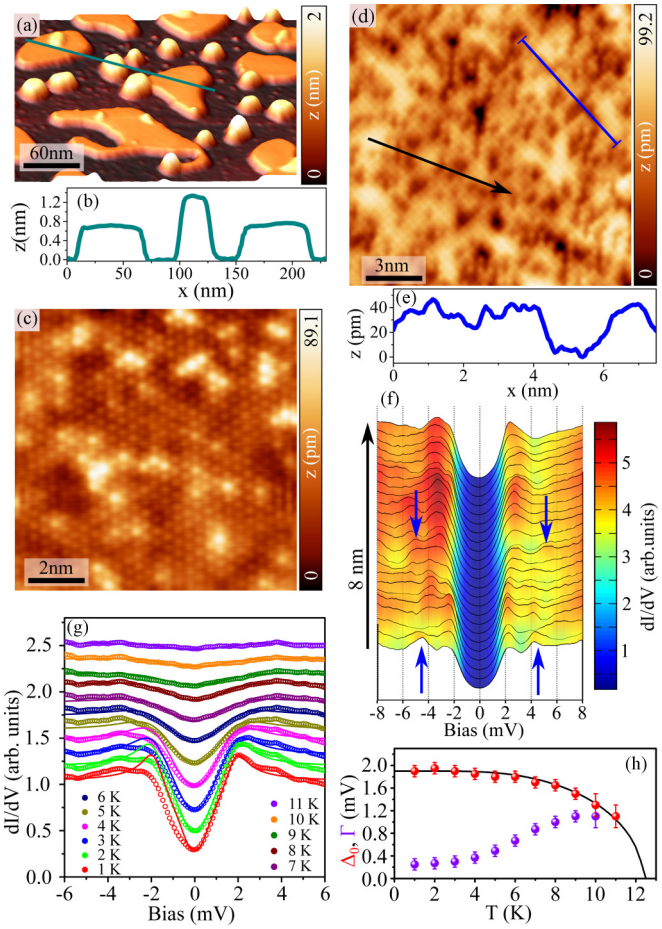

FIG. 1. Growth and superconductivity of $FeSe_xTe_{1-x}$ on $Bi_2Se_{1.2}Te_{1.8}$. (a) The 3D view of a 300 nm × 300 nm constant-current STM topograph showing islands of $FeSe_xTe_{1-x}$ ($V = -600$ mV, $I_s =$ 30 pA). (b) Height profile along the line shown in (a). (c) Constant-current topograph acquired on the substrate ($V = -5.7$ mV, $I_s =$ 200 pA). The image is a composition of the original and a Fourier filtered topograph to enhance the atomic resolution. (d) Constant-current topograph acquired on the single layer of $FeSe_xTe_{1-x}$ ($x \sim 0.5, V = 200$ mV, $I_s = 3$ nA). (e) Height profile along the blue line shown in (d). (f) Tunneling spectra acquired at $T = 1.1$ K along the black arrow shown in (d). Blue arrows show the positions of second coherence peaks originating from a large gap structure characteristic for Te-rich sites. (g) Temperature dependent and background corrected spectra along with anisotropic BCS fits. Here the fits are done on the positive side of the spectra. Spectra are shifted vertically for clarity. The degree of anisotropy used for all temperatures is $a = 0.38$. (h) Temperature dependence of the superconducting energy gap (Δ_0) (red) and the Dynes broadening parameter (Γ) (purple). The solid black curve represents the temperature evolution of the energy gap $\Delta(T)$ expected within BCS theory.

III. RESULTS AND DISCUSSION

Figure 1(a) shows a three-dimensional (3D) view of a large area scanning tunneling microscope (STM) topograph where we see the growth of large is lands of MLs and small islands of two layers of $FeSe_xTe_{1-x}$ on the substrate [30]. The line profile across three islands [Fig. 1(b)] indicates a height of the ML above the substrate of ∼0.71 nm, which is slightly larger than the corresponding bulk lattice constant (0.607 nm) [31]. The height of the second layer with respect to the first layer is ∼0.6 nm. Constant current topographs with atomic resolution taken on the substrate depict the hexagonal atomic structure [Fig. 1(c)], while the STM topograph acquired at the center of one of the islands of $FeSe_xTe_{1-x}$ [Fig. 1(d)] shows the tetragonal atomic lattice, which resembles the bulk-like atomic structure reported earlier [32]. Here, Te appears brighter than Se atoms, and by counting the number of each species we estimate the composition as $\sim(50 \pm 10)\,\%$ Te and Se each, which is the optimal doping for highest T_c in the corresponding bulk system (Fig. 4). From the line profile (blue) shown in Fig. 1(e), the height difference between Te and Se atoms is $\sim(32 \pm 10)$ pm. From a Fourier analysis of the STM data on different islands, we extract an in-plane lattice constant of (0.38 ± 0.002) nm, which is close to that of the bulk material [31]. Figure 1(f) shows the dI/dV spectra acquired along a line of 8 nm length, starting with a Te-rich site displaying a fully developed gap at the Fermi level (E_F) characteristic for superconductivity. It is interesting to note that on Te-rich sites, we observe two gap features with two coherence peaks that appear symmetrically around E_F at (2.1 ± 0.5) mV and (4.5 ± 0.5) mV (Fig. 5), which are consistent with earlier STS results and ARPES measurements on the bulk system [33,34]. In Fig. 1(g), we show the temperature evolution of the spectra, where the spectra are corrected for the background by dividing all the spectra by the spectrum at 12 K. The spectrum at 12 K is chosen because we see only a large V-shaped background that does not change at higher temperatures. The spectra reveal that the gap becomes shallower with increasing temperature and vanishes around 12 K. We see a slight asymmetry in the spectra around zero bias; therefore, to get a quantitative estimate about the superconducting T_c, we fit only the positive side of the conductance spectra within the Bardeen-Cooper-Schrieffer (BCS) framework along with the Dynes broadening parameter [29]. To appropriately model this data (Fig. 6), we have to assume a considerable anisotropy in the energy gap, given as $\Delta(\theta) = \Delta_0[1 + a(\cos 2\theta - 1)]$ with the maximum value of the energy gap Δ_0 and the degree of gap anisotropy a and a comparatively large Dynes broadening parameter Γ. The fits are shown by corresponding solid lines [Fig. 1(g)], where the degree of anisotropy used for best fits at all temperatures is $a = 0.38$. Figure 1(h) depicts the temperature evolution of Δ_0 and Γ. The evolution of Δ_0 follows the solid black curve, which is expected from BCS theory [35] with $T_c = 12.5$ K, while we observe that Γ increases with temperature. It should be noted that the choice of the two-fold anisotropy of the gap function is not unique here (Fig. 6) but is substantiated by the quasiparticle interference (QPI) shown below. The large Γ value for our system indicates short-lived Bogoliubov quasiparticles, consistent with the large pair breaking scattering known in the corresponding bulk system [36] and possibly resulting in a strong scattering seen in our system as discussed below. However, we cannot rule out that there is another contribution to Γ from quasiparticle relaxations at the interface of the film and the substrate [37].

To study the spatial evolution of the superconductivity, we acquired dI/dV spectra at $T = 1.1$ K on 60 × 60 pixels over a 20 nm x 20 nm area [Fig. 2(a)]. Figures 2(b)–2(d) show characteristic spectra acquired at three different locations

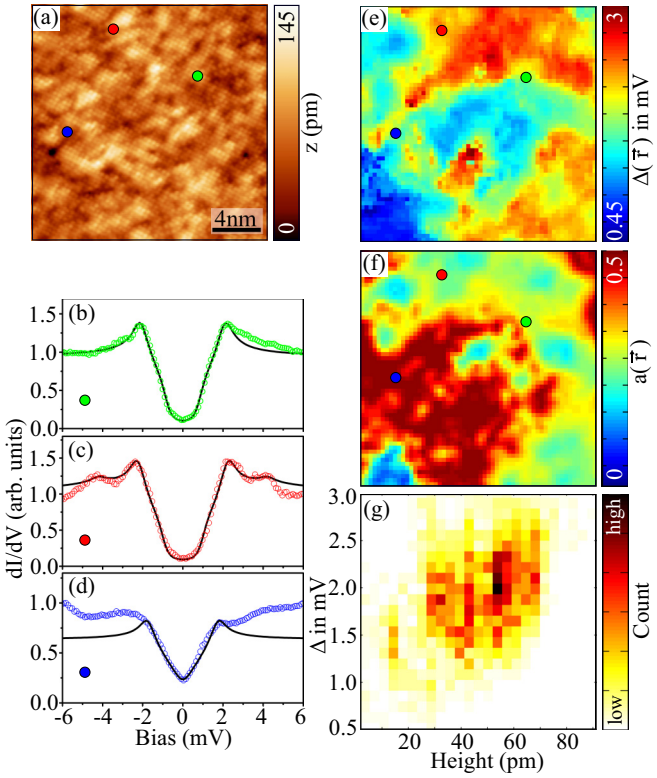

FIG. 2. Inhomogeneities of gap structure, gap size, and gap anisotropy. (a) Constant current STM topograph showing an area of a single layer of $FeSe_xTe_{1-x}$, where the spectroscopic data of this figure has been measured. (b)–(d) Tunneling conductance spectra (markers) acquired at $T = 1.1$ K at the three different locations on $FeSe_{0.5}Te_{0.5}$, indicated by correspondingly colored markers in (a), (e), and (f). The continuous black curves plotted along with the measured spectra represent fits using an anisotropic gap function (see text). Fit parameters: (b) $\Delta_0 = 2.1$ meV,$a = 0.3$,$\Gamma = 0.14$ meV; (c) $\Delta_{0L} = 4.2$ meV,$\Delta_{0S} = 2.25$ meV,$a = 0.28$,$\Gamma = 0.14$ meV, $\sigma = 0.15$; (d) $\Delta_0 = 1.75$ meV,$a = 0.5$,$\Gamma = 0.14$ meV. (e) Spatial evolution of the superconducting gap over the area of (a) obtained by fitting each spectrum of a 60×60 pixel spectroscopic field employing an anisotropic gap in the BCS density of states (BCS-DOS). The fitting procedure is applied only to the positive side of the spectra. (f) Corresponding anisotropy map obtained from the fits. (g) The 2D histogram of Δ_0 and topographic height plotted as intensity map.

[shown in Fig. 2(a) with corresponding circles]. These spectra are corrected for the background using the spatially averaged spectrum at 12 K. We observe an inhomogeneity in the gap, which is also visible in the tunneling conductance maps at different bias values (Fig. 7). The spectra in Fig. 2(b) and Fig. 2(d) are fitted with single anisotropic energy gaps shown by black curves, where the corresponding fit parameters are given in the caption. The spectrum in Fig. 2(c) is a characteristic Te-rich site, as discussed earlier, and can be fitted with a two-gap model using the equation $G = \sigma G_L + (1 - \sigma)G_S$, where $G_L(G_S)$ is the differential conductance simulated using a large (small) energy gap Δ_{0L} (Δ_{0S}), σ is the spectral weight for the large gap, and G is the resulting conductance [38]. Note that we used the same degree of anisotropy and lifetime broadening parameters for both gaps. It is evident from these fits that we are able to appropriately capture the spectral shape within the anisotropic gap. To analyze the data acquired on the entire area, we use an automatic least-squares fitting algorithm employing an anisotropic gap function (Fig. 8). For simplicity, we leave out the larger gap in this analysis and fit the spectra using only positive part of the conductance spectra. The resulting energy gap values are plotted as a map in Fig. 2(e). We see a large variation in the gap values ranging from 0.45 meV to 3 meV and formation of patches with irregular shapes. Figure 2(f) shows the anisotropy map obtained from the corresponding fits. Here, $0 < a < 0.5$ represents an anisotropic, nodeless gap, while $a = 0.5$ corresponds to a nodal gap. Obviously, there is a quite large spatial variation in the gap structure, which changes from nodeless to nodal-like, on the length scale of only 10–15 nm. In Fig. 2(g), we plot a two-dimensional (2D) histogram of the gap magnitude and the corresponding heights measured in the STM topograph, where the latter reflects the local chemical composition of the $FeSe_{0.5}Te_{0.5}$ film. We find only a very weak correlation and therefore conclude that the large inhomogeneity in the gap magnitude is not straightforwardly connected to the chemical disorder. While there are only two 10–15 nm large domains with a completely evolved superconducting gap in the image area of Fig. 2(e), the Se-rich and Te-rich patches, which are much smaller in size (1–2 nm), are uniformly spread over the measured area [Fig. 2(a)].

A similar behavior is well known from high-T_c cuprates [39] and disordered s-wave SCs [40,41]. In such disordered SCs, the spontaneous formation of large superconducting domains is observed, which are uncorrelated with the disorder, which has a much smaller characteristic length scale. This scenario is further supported for our system by the temperature dependent spectroscopy, where we track the spatial evolution of dI/dV spectra as a function of temperature (Fig. 9). We see that inhomogeneous spectra evolve smoothly and segregate spontaneously to form patches with large gap magnitude, indicated by low zero bias conductance (Fig. 9). This clearly suggests a breakdown of long-range coherence at elevated temperatures through thermal phase fluctuations [42], which might be additionally affected by possible quantum phase fluctuations of the quasi-2D system at low temperatures. The intrinsic disorder, which affects the superconductivity in the system we investigate here, is of two kinds. First, the anion species (Se/Te) has a local effect on the electronic properties [43], which leads to disorder on a length scale of 1–2 nm. Second, additional disorder is coming from the charge transfer between the substrate and the film [25] in combination with the doping disorder in the substrate. The length scale of the corresponding disorder potential is on the order of $\sim$10 nm, as estimated from the carrier concentration in the substrate [28]. It would be therefore interesting to study this system under different growth conditions, including a variation of the Se/Te ratio, the substrate doping, and different annealing times. It would also be interesting to study the role of interstitial excess Fe atoms on the electronic inhomogeneity, which are otherwise not seen in our system. So far, our results motivate further theoretical studies to explore disordered superconductivity in FeSCs.

Next, to get both real space and momentum space information on the electronic structure, we acquired spectroscopy maps within an energy range of -5 mV to 5 mV over 512×512 pixels on a 25 nm $\times$ 25 nm area (Fig. 10). The tunneling

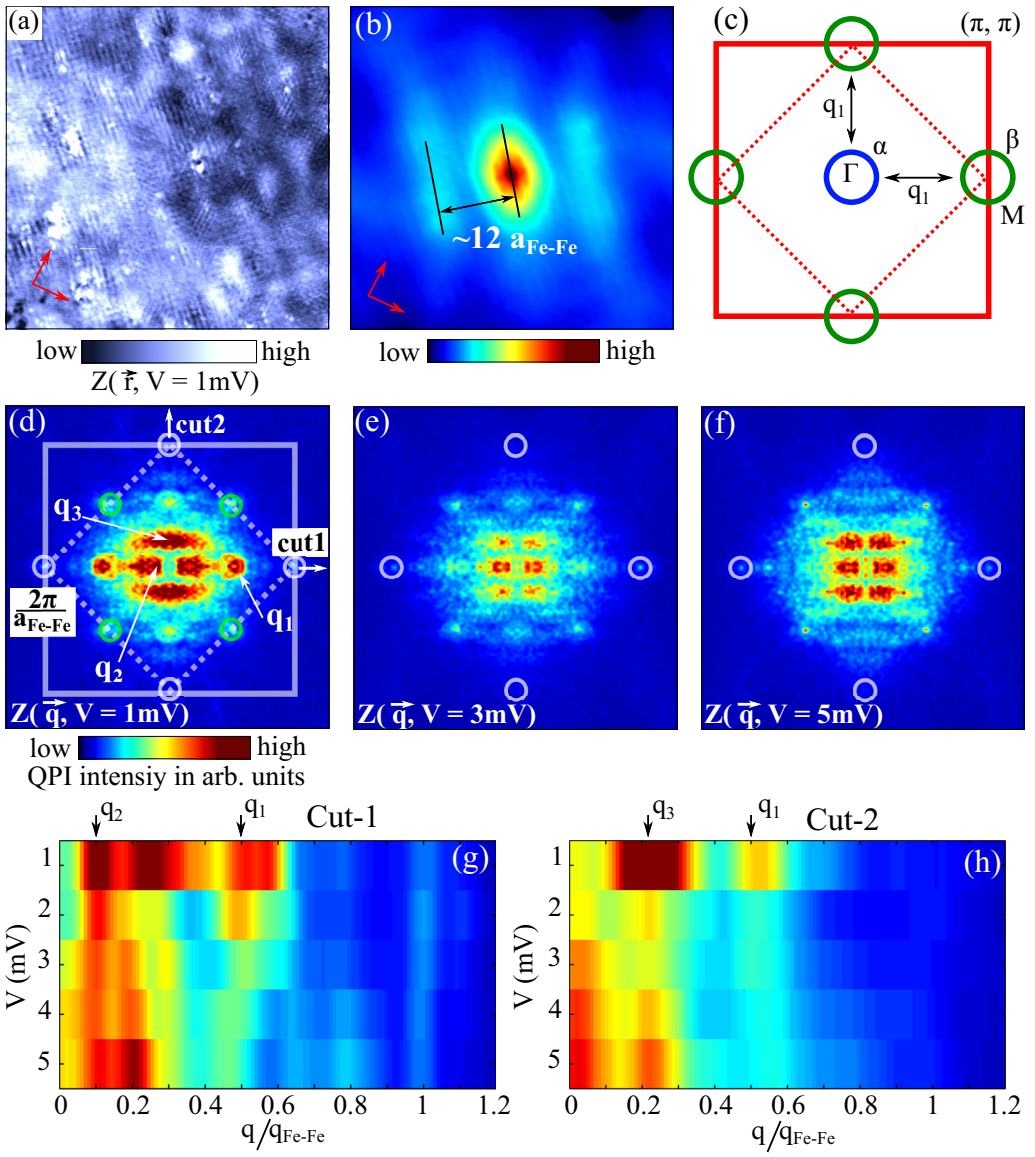

FIG. 3. Two-fold symmetry in quasiparticle interference analyzed by FT-STS (a) Z map, obtained by taking the ratio of conductance maps over an area of 25 nm × 25 nm at 1 mV and −1 mV. (b) Autocorrelation of (a). (c) Simplified schematic diagram of the unfolded BZ of the unit cell with a single Fe atom. The blue circle at Γ and the green circles at the M points represent the expected hole and electron pockets, respectively. (d)–(f) Fourier transforms of Z maps at the various indicated bias values. Light green circles in (d) represent Bragg peaks due to Se/Te atoms, while white circles in each panel represent Bragg peaks due to Fe atoms. (g), (h) Dispersions of QPI vectors along Cuts 1 and 2 shown in (d), which represent the high symmetry directions along Fe-Fe bonds. The corresponding origins of the scattering intensities are indicated in (d).

conductance map at $V = 1$ mV again reveals the strong gap inhomogeneity owing to the anticorrelation between the conductance at $V = 1$ mV and the energy gap (Δ) (Fig. 11). Moreover, QPI of Bogoliubov quasiparticles is visible by a weaker intensity modulation of the contrast having different wavelengths. To enhance the visibility of these QPI patterns and to minimize set-point effects, we take the map of the ratio defined as $Z(\vec{r},V) = g(\vec{r},V)/g(\vec{r},-V)$ [44]. Figure 3(a) shows such a Z map at $V = 1$ mV. Here, we see a unidirectional stripelike pattern, i.e., C_2 symmetry of the electronic structure. It is further evident in the corresponding autocorrelation map in Fig. 3(b), where the periodic order corresponding to a distance of $\sim 12\, a_{\text{Fe-Fe}}$ is visible in a direction along the Fe-Fe nearest neighbors. The profound C_2 symmetry of the electronic structure is also visible when we plot Fourier transform (FT) images of the Z maps (see Fig. 12 for raw data). Figures 3(d)–3(f) show such FT images at different bias voltages in the gap region, where we observe stripe-shaped QPI patterns elongated along one of the two Fe Bragg peaks, demonstrating again the C_2 symmetry of the electronic structure. To illustrate the dispersion of the different QPI scattering vectors, we plot in Figs. 3(g) and 3(h) the line cuts through the FT images of the Z maps at different bias voltages along the two orthogonal directions from the center through the Fe Bragg peaks. We see both dispersing and nondispersing QPI scattering vectors $\mathbf{q}$ as a function of energy.

Cut 1 shows two noticeable intensities: $\mathbf{q}_1 \sim 0.5 \times \mathbf{q}_{\text{Fe-Fe}}$ at $V = 1$ mV, which disperses to slightly lower $\mathbf{q}$ for increasing energy, and $\mathbf{q}_2 \sim 0.09 \times \mathbf{q}_{\text{Fe-Fe}}$, which does not disperse. Cut 2, shown in Fig. 2(h), also displays two major intensities: $\mathbf{q}_1 \sim 0.5 \times \mathbf{q}_{\text{Fe-Fe}}$ at $V = 1$ mV, which disperses to slightly higher $\mathbf{q}$ for increasing energy, and $\mathbf{q}_3 \sim 0.21 \times \mathbf{q}_{\text{Fe-Fe}}$, which again does not disperse and could possibly originate from intraband scattering of the α bands [19]. The dispersive scattering vectors $\mathbf{q}_1$ in the two different cuts are most probably corresponding to the interband scattering between electron and hole bands, indicated in Fig. 3(c), which have been also observed in bulk $FeSe_{0.4}Te_{0.6}$ [14]. However, note that in our case, a charge transfer between the substrate and the $FeSe_{0.5}Te_{0.5}$ film could shift the energy of the bands such that we do not *a priori* know the exact size of these scattering vectors. More importantly, the nondispersive scattering vectors $\mathbf{q}_2$ and $\mathbf{q}_3$ strongly indicate the breaking of C_4 symmetry. Interestingly, $\mathbf{q}_2$ represents the same ordering with a periodicity of $\sim 12\, a_{\text{Fe-Fe}}$, as seen in the autocorrelation of the real space Z map [Fig. 3(b)]. It should also be noted that even though we observe inhomogeneity in the superconducting energy gap, a similar C_2 symmetry is observed locally in both the low gap and high gap region in Fig. 3(a), which implies two-fold anisotropy in the gap structure.

We finally discuss the possible origin of the reduction to C_2 symmetry. Interestingly, a very similar symmetry reduction in the autocorrelation images and QPI patterns, often referred to as nematicity, has been observed in the electronic structure of bulk Fe pnictides [45,46] and bulk $FeSe_{0.4}Te_{0.6}$ [19]. For these systems, it has been shown that strong spin-orbit interaction can break the orbital degeneracy between the d_{xz} and d_{yz} orbitals [4,47], which leads to orbital splitting between the two corresponding bands [5]. Correspondingly, based on a STM study of bulk $FeSe_{0.4}Te_{0.6}$ [19], it was proposed that this orbital ordering is responsible for the symmetry breaking observed in the spectral maps. Using their result of the scattering vector as a function of the orbital splitting energy, we estimate splitting of 19.5 mV for $\mathbf{q}_2$ (Fig. 13), which is comparable to the one reported by ARPES studies of bulk $FeSe_{0.4}Te_{0.6}$ [5]. Therefore, our results indicate that the observed $12\, a_{\text{Fe-Fe}}$ periodicity corresponding to $\mathbf{q}_2$ could be a result of orbital ordering.

IV. CONCLUSION

In summary, we have successfully grown MLs of FeSCs on topological insulators and characterized the local electronic properties. We describe the spectra using an anisotropic energy gap and find strong inhomogeneities, unlike in the corresponding bulk system. The observed inhomogeneities are most probably due to the emergent nature of superconductivity, analogous to disordered s-wave SCs. We propose a two-fold anisotropic gap structure based on the observation of a pronounced C_2 symmetry in the QPI patterns, which probably is the result of a spin-orbital coupling as compared to the corresponding bulk material.

ACKNOWLEDGMENTS

We are indebted to Alexander Balatsky, Christopher Triola, Tim O. Wehling, and Udai R. Singh for valuable discussions. This paper has primarily been supported by the ERC Advanced Grant ASTONISH (No. 338802). L.C., Ph.H., and J.W. acknowledge support through the Deutsche Forschungsgemeinschaft (DFG) priority program SPP1666 (Grant No. WI 3097/2), T.H. acknowledges support by the DFG under Grant No. HA 6037/2-1, and Ph.H. acknowledge support by VILLUM FONDEN via Center of Excellence for Dirac Materials (Grant No. 11744). We thank the Danish National Research Foundation (Center for Materials Crystallography, Grant No. DNRF93) for supporting the bulk crystal growth.

A.K. and S.M. contributed equally to this work.

APPENDIX

A. Nanoscale chemical composition

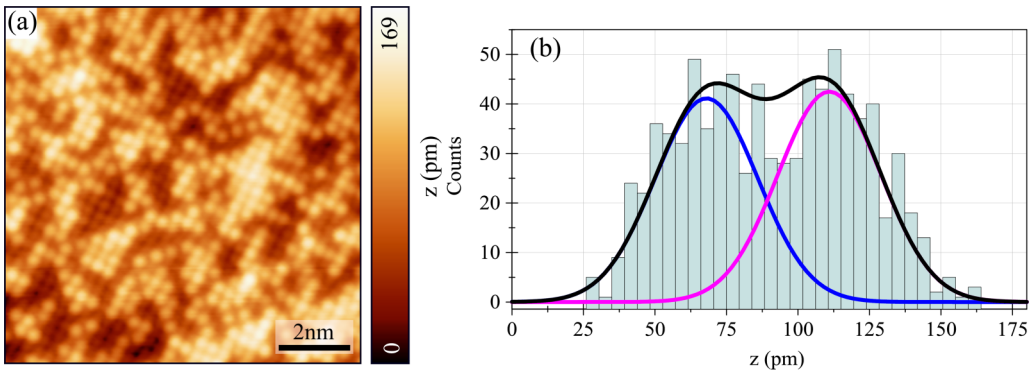

FIG. 4. (a) Constant current STM topograph acquired on a single layer of $FeSe_xTe_{1-x}$ ($V = 60$ mV; $I_s = 200$ pA). (b) Histogram of the z values of the centers of atoms in (a). The black curve, which is the sum of the blue and pink Gaussian functions, has been fitted to the histogram. The blue and the pink curve correspondingly represent the Se and Te atoms, respectively. The composition of Se and Te calculated by using the area below the two curves is 48% and 52%, respectively, with an error of 6%.

B. Two gap features on Te-rich sites

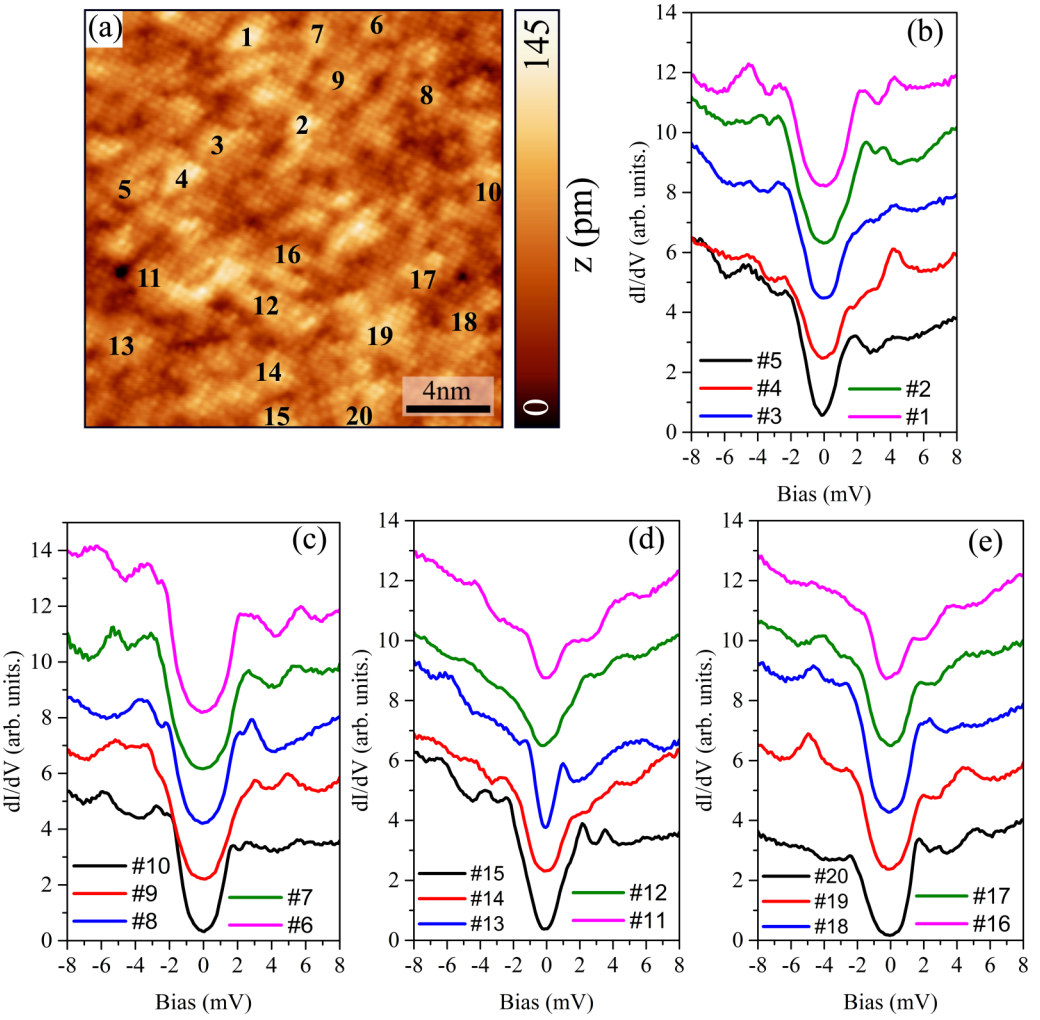

FIG. 5. (a) Constant current STM topograph acquired on a single layer of $FeSe_xTe_{1-x}$ ($V = 10\,\text{mV}$; $I_s = 400\,\text{pA}$). Numbers indicate the Te-rich sites where spectroscopic data was acquired. The raw spectra corresponding to these numbered positions are plotted in (b)–(e). All the spectra show two gap features with two coherence peaks that appear symmetrically around E_F at $(2.1 \pm 0.5)\,\text{mV}$ and $(4.5 \pm 0.5)\,\text{mV}$.

C. Modeling STS data using an anisotropic energy gap

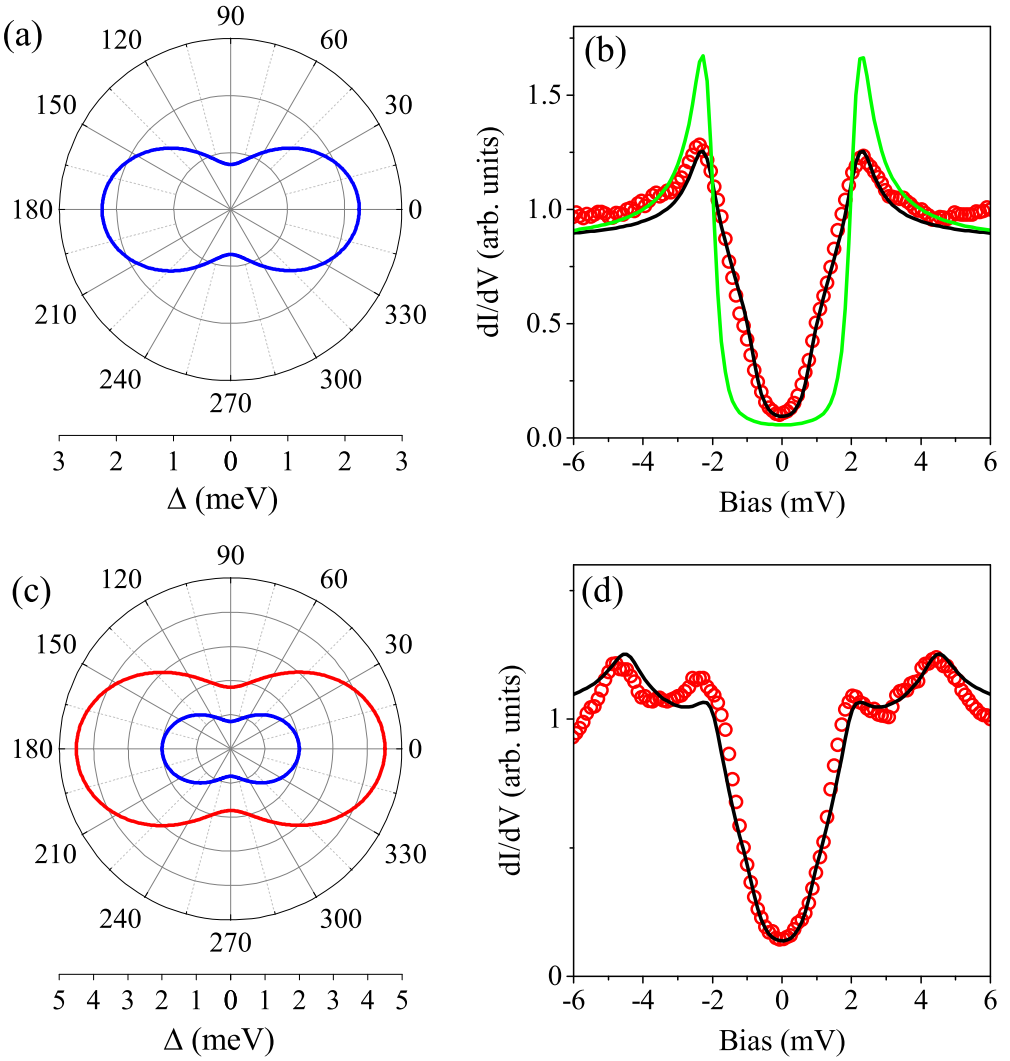

FIG. 6. (a) Anisotropic gap function given by $\Delta(\theta) = \Delta_0[1 + a(\cos 2\theta - 1)]$, where Δ_0 is the maximum value of the energy gap and a represents the degree of gap anisotropy. In this case, $\Delta_0 = 2.25$ meV and $a = 0.325$ was assumed. (b) Typical dI/dV spectrum (red circles). The green curve represents a fit using the BCS-Dynes density of states: $N(E) = N_n(E_F) \cdot \mathrm{Re}[\frac{E+i\Gamma}{\sqrt{(E+i\Gamma)^2-\Delta^2}}]$, where $\Delta = 2.1$ meV and $\Gamma = 0.14$ meV, whereas the black curve denotes the fit using the BCS-Dynes density of states $N(E) = N_n(E_F) \cdot \mathrm{Re}[\frac{E+i\Gamma}{\sqrt{(E+i\Gamma)^2-\Delta(\theta)^2}}]$ (black curve) [29] employing an anisotropic energy gap $\Delta(\theta)$ shown in (a) with the Dynes broadening parameter $\Gamma = 0.14$ meV. (c) Anisotropic gap function for two gaps with $\Delta_{0L} = 4.5$ meV, $\Delta_{0S} = 2$ meV, and $a = 0.3$, where the subscripts L and S stand for large and small gaps, respectively. (d) Typical dI/dV spectrum (red circles) taken at a Te-rich site. The black curve plotted together with the data represents a fit using a two gap model based on the equation $G = \sigma G_L + (1 - \sigma)G_S$ [38], where $G_L(G_S)$ are the differential conductances simulated using large (small) energy gaps Δ_{0L} (Δ_{0S}), σ is the spectral weight due to the large gap, and G is the resulting conductance. The used anisotropic energy gaps are shown in (c), while the other fit parameters are $\sigma = 0.4$ and $\Gamma = 0.22$ meV. It should be noted that the choice of the anisotropic gap function is not unique. We get the same results if we replace the $\cos 2\theta$ term in the gap function by $\cos 4\theta$.

D. Tunneling conductance maps

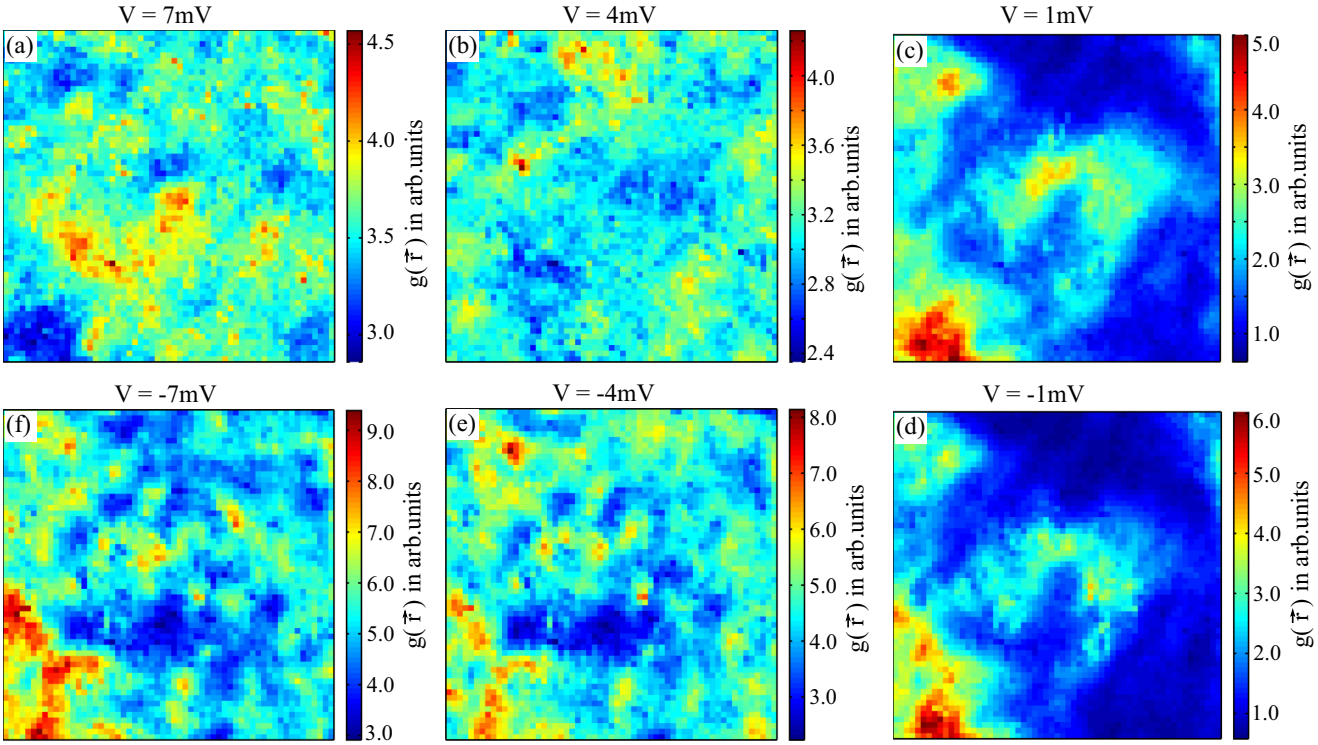

FIG. 7. Tunneling conductance maps at various bias voltages, which are derived from the dI/dV spectra taken on 60 $\times$ 60 pixels over a 20 nm $\times$ 20 nm area. The inhomogeneity in the spectra within the gap region is apparent from the maps.

E. Spectra along with fitting

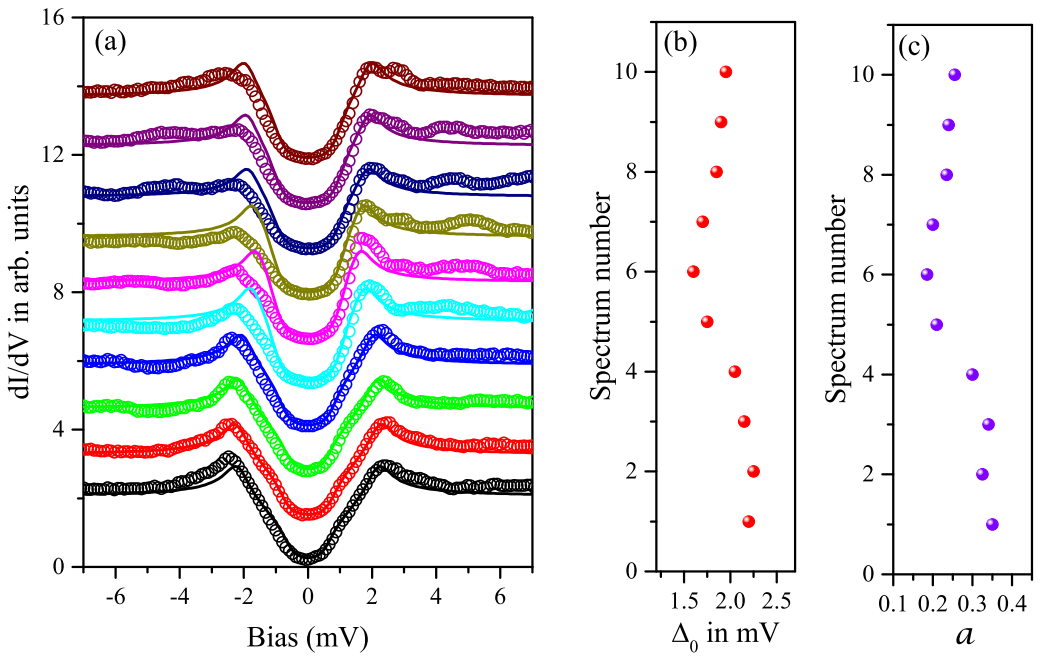

FIG. 8. (a) Tunneling spectra (markers) plotted along with the fits using the model with a single anisotropic gap function (lines). Fit procedure is applied on the positive side of the conductance spectra, as described in the text. (b) Superconducting energy gap (Δ_0) corresponding to the fits shown in (a). (c) The degree of anisotropy a, obtained from the corresponding fits shown in (a).

F. Temperature evolution of tunneling conductance spectra

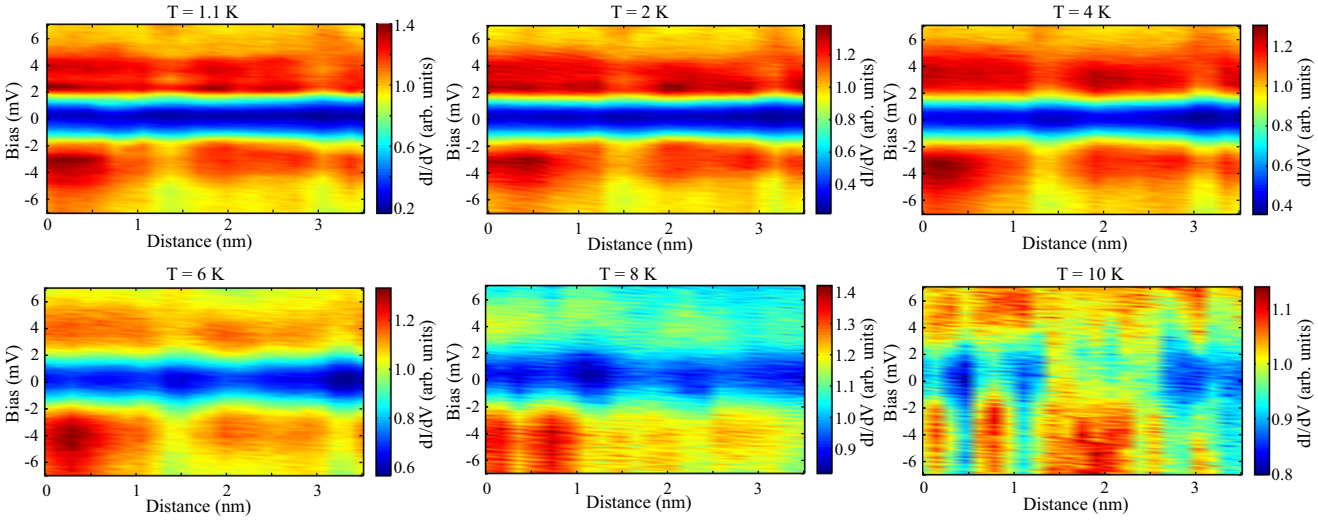

FIG. 9. Lateral evolution of tunneling spectra over a 3.5 nm long line as a function of temperature. We observe that the spectra evolve smoothly, and at high temperature ($T = 10$ K) the local superconducting correlations persist, as seen by the formation of blue patches related to the gap in dI/dV.

G. Tunneling conductance maps corresponding to QPI data

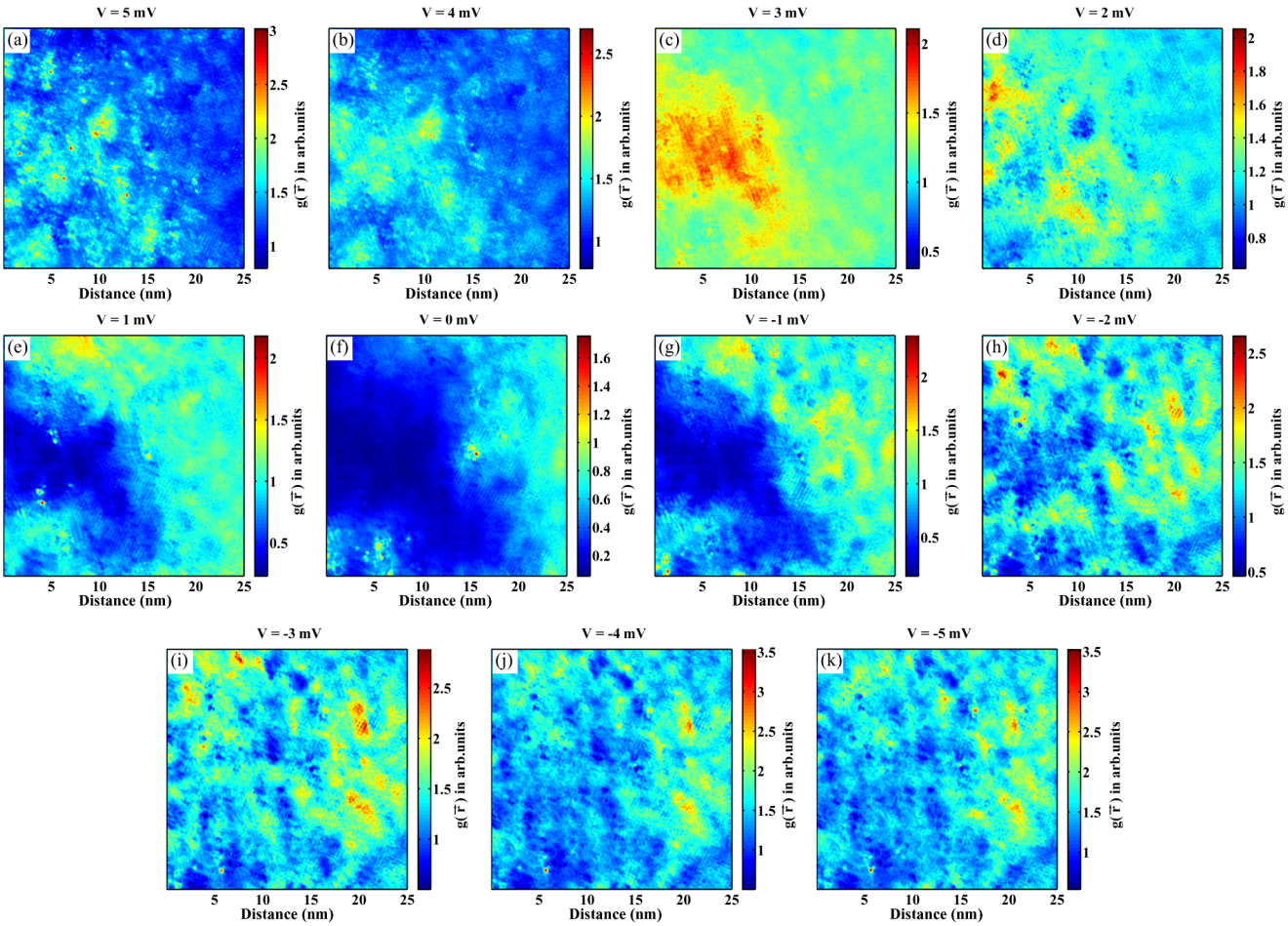

FIG. 10. Tunneling conductance maps at various bias voltages, which are derived from the dI/dV spectra taken on 512×512 pixels over a 25 nm $\times$ 25 nm area. The inhomogeneity in the superconducting properties is apparent from the maps at low bias voltages

H. Anticorrelation between energy gap (Δ) and differential tunneling conductance at $V = 1$ mV

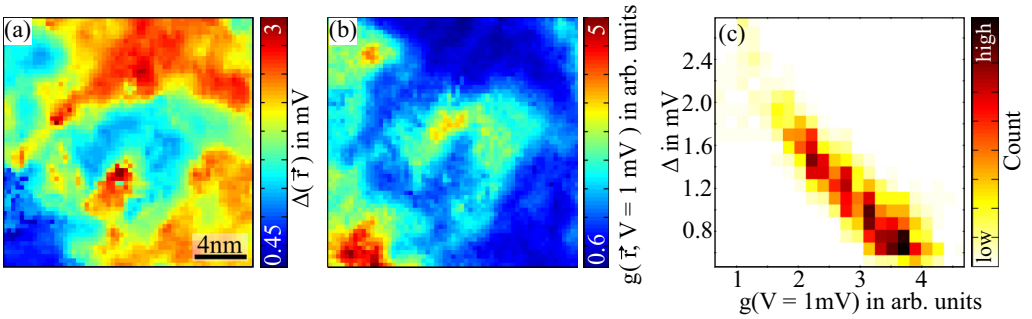

FIG. 11. (a) Spatial evolution of the superconducting energy gap [same data as in Fig. 2(e) of the main text]. (b) Corresponding conductance map at $V = 1$ mV. (c) The 2D histogram of the superconducting energy gap ($\triangle$) and the corresponding conductance value g at $V = 1$ mV, plotted as intensity map. The negative slope here represents an anticorrelation between $\triangle$ and $g(\vec{r}, V = 1$ mV).

I. Fourier transform analysis

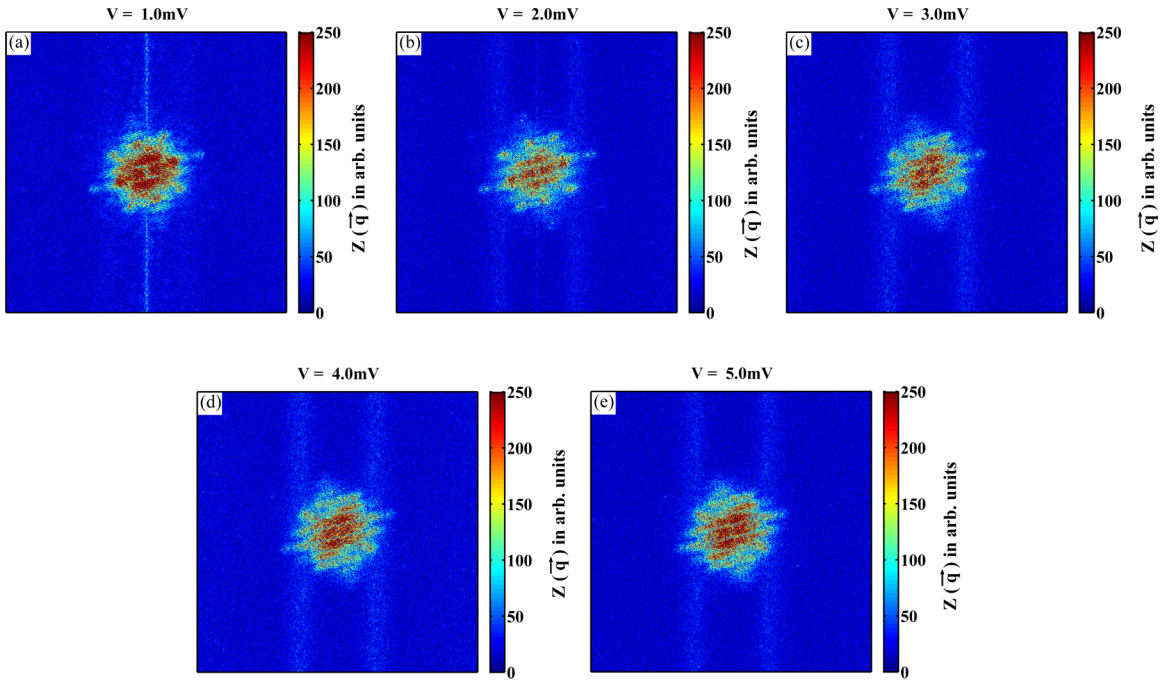

FIG. 12. Fourier transforms of Z maps at various bias values. Here each plot is obtained using fast Fourier transform analysis of Z maps and then subtracting the central core to enhance the visibility of relevant **q** vectors. For further analysis of different quasiparticle structures, the data is symmetrized along a high symmetry axis, i.e., along Fe-Fe bonds, and low pass filtered to reduce the noise. The resulting data is presented in Fig. 3 of the main text.

J. Estimation of orbital splitting energy

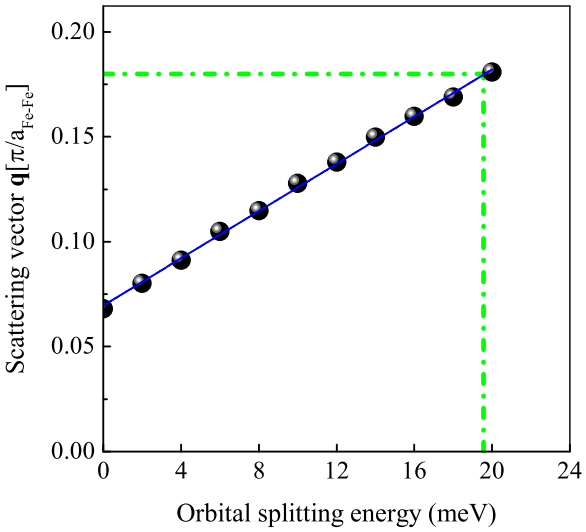

FIG. 13. The plots represent the data extracted from Ref. [19], where the authors calculated the orbital splitting energy as a function of the dominant scattering vector **q**, corresponding to symmetry breaking states, employing the joint density of states approach. Using their results, we estimate orbital splitting energies of 19.5 meV in our system, corresponding to the observed scattering vector $\mathbf{q}_2 = 0.18\,\pi/a_{\text{Fe-Fe}}$.

[1] Y. Kamihara, T. Watanabe, M. Hirano, and H. Hosono, J. Am. Chem. Soc. **130**, 3296 (2008).

[2] A. V. Chubukov, Annu. Rev. Condens. Matter Phys. **3**, 57 (2012).

[3] T. D. Stanescu, V. Galitski, and S. Das Sarma, Phys. Rev. B **78**, 195114 (2008).

[4] P. D. Johnson, H.-B. Yang, J. D. Rameau, G. D. Gu, Z.-H. Pan, T. Valla, M. Weinert, and A. V. Fedorov, Phys. Rev. Lett. **114**, 167001 (2015).

[5] H. Miao, L.-M. Wang, P. Richard, S.-F. Wu, J. Ma, T. Qian, L.-Y. Xing, X.-C. Wang, C.-Q. Jin, C.-P. Chou, Z. Wang, W. Ku, and H. Ding, Phys. Rev. B **89**, 220503 (2014).

[6] K.-W. Yeh, T.-W. Huang, Y.-L. Huang, T.-K. Chen, F.-C. Hsu, P. M. Wu, Y.-C. Lee, Y.-Y. Chu, C.-L. Chen, J.-Y. Luo, D.-C. Yan, and M.-K. Wu, EPL **84**, 37002 (2008).

[7] Y. Han, W. Y. Li, L. X. Cao, X. Y. Wang, B. Xu, B. R. Zhao, Y. Q. Guo, and J. L. Yang, Phys. Rev. Lett. **104**, 017003 (2010).

[8] Y. Imai, T. Akiike, M. Hanawa, I. Tsukada, A. Ichinose, A. Maeda, T. Hikage, T. Kawaguchi, and H. Ikuta, Appl. Phys. Express **3**, 43102 (2010).

[9] W. Si, Z. W. Lin, Q. Jie, W. G. Yin, J. Zhou, G. Gu, P. D. Johnson, and Q. Li, Appl. Phys. Lett. **95**, 52504 (2009).

[10] E. Bellingeri, I. Pallecchi, R. Buzio, A. Gerbi, D. Marrè, M. R. Cimberle, M. Tropeano, M. Putti, A. Palenzona, and C. Ferdeghini, Appl. Phys. Lett. **96**, 102512 (2010).

[11] S. Medvedev, T. M. McQueen, I. A. Troyan, T. Palasyuk, M. I. Eremets, R. J. Cava, S. Naghavi, F. Casper, V. Ksenofontov, G. Wortmann, and C. Felser, Nat. Mater. **8**, 630 (2009).

[12] F. Li, H. Ding, C. Tang, J. Peng, Q. Zhang, W. Zhang, G. Zhou, D. Zhang, C.-L. Song, K. He, S. Ji, X. Chen, L. Gu, L. Wang, X.-C. Ma, and Q.-K. Xue, Phys. Rev. B **91**, 220503 (2015).

[13] Q.-Y. Wang, Z. Li, W.-H. Zhang, Z.-C. Zhang, J.-S. Zhang, W. Li, H. Ding, Y.-B. Ou, P. Deng, K. Chang, J. Wen, C.-L. Song, K. He, J.-F. Jia, S.-H. Ji, Y.-Y. Wang, L.-L. Wang, X. Chen, X.-C. Ma, and Q.-K. Xue, Chinese Phys. Lett. **29**, 37402 (2012).

[14] T. Hanaguri, S. Niitaka, K. Kuroki, and H. Takagi, Science **328**, 474 (2010).

[15] T. J. Liu, J. Hu, B. Qian, D. Fobes, Z. Q. Mao, W. Bao, M. Reehuis, S. A. J. Kimber, K. Prokes, S. Matas, D. N. Argyriou, A. Hiess, A. Rotaru, H. Pham, L. Spinu, Y. Qiu, V. Thampy, A. T. Savici, J. A. Rodriguez, and C. Broholm, Nat. Mater. **9**, 716 (2010).

[16] I. I. Mazin and D. J. Singh, arXiv:1007.0047.

[17] P. J. Hirschfeld, D. Altenfeld, I. Eremin, and I. I. Mazin, Phys. Rev. B **92**, 184513 (2015).

[18] C.-L. Song, Y.-L. Wang, P. Cheng, Y.-P. Jiang, W. Li, T. Zhang, Z. Li, K. He, L. Wang, J.-F. Jia, H.-H. Hung, C. Wu, X. Ma, X. Chen, and Q.-K. Xue, Science **332**, 1410 (2011).

[19] U. R. Singh, S. C. White, S. Schmaus, V. Tsurkan, A. Loidl, J. Deisenhofer, and P. Wahl, Sci. Adv. **1**, e1500206 (2015).

[20] S.-H. Baek, D. V. Efremov, J. M. Ok, J. S. Kim, J. van den Brink, and B. Büchner, Nat. Mater. **14**, 210 (2014).

[21] H. Kontani and S. Onari, Phys. Rev. Lett. **104**, 157001 (2010).

[22] H. C. Xu, X. H. Niu, D. F. Xu, J. Jiang, Q. Yao, M. Abdel-Hafiez, D. A. Chareev, A. N. Vasiliev, R. Peng, and D. L. Feng, Phys. Rev. Lett. **117**, 157003 (2016).

[23] K. Okazaki, Y. Ito, Y. Ota, Y. Kotani, T. Shimojima, T. Kiss, S. Watanabe, C.-T. Chen, S. Niitaka, T. Hanaguri, H. Takagi, A. Chainani, and S. Shin, Phys. Rev. Lett. **109**, 237011 (2012).

[24] B. Zeng, G. Mu, H. Q. Luo, T. Xiang, I. I. Mazin, H. Yang, L. Shan, C. Ren, P. C. Dai, and H.-H. Wen, Nat. Commun. **1**, 112 (2010).

[25] A. Eich, N. Rollfing, F. Arnold, C. Sanders, P. R. Ewen, M. Bianchi, M. Dendzik, M. Michiardi, J.-L. Mi, M. Bremholm,

D. Wegner, P. Hofmann, and A. A. Khajetoorians, Phys. Rev. B **94**, 125437 (2016).
[26] L. Fu and C. L. Kane, Phys. Rev. Lett. **100**, 096407 (2008).
[27] H.-H. Sun, K.-W. Zhang, L.-H. Hu, C. Li, G.-Y. Wang, H.-Y. Ma, Z.-A. Xu, C.-L. Gao, D.-D. Guan, Y.-Y. Li, C. Liu, D. Qian, Y. Zhou, L. Fu, S.-C. Li, F.-C. Zhang, and J.-F. Jia, Phys. Rev. Lett. **116**, 257003 (2016).
[28] J.-L. Mi, M. Bremholm, M. Bianchi, K. Borup, S. Johnsen, M. Søndergaard, D. Guan, R. C. Hatch, P. Hofmann, and B. B. Iversen, Adv. Mater. **25**, 889 (2013).
[29] P. Löptien, L. Zhou, A. A. Khajetoorians, J. Wiebe, and R. Wiesendanger, J. Phys. Condens. Matter **26**, 425703 (2014).
[30] S. Manna, A. Kamlapure, L. Cornils, T. Hänke, E. M. J. Hedegaard, M. Bremholm, B. B. Iversen, P. Hofmann, J. Wiebe, and R. Wiesendanger, Nat. Commun. **8**, 14074 (2017).
[31] B. C. Sales, A. S. Sefat, M. A. McGuire, R. Y. Jin, D. Mandrus, and Y. Mozharivskyj, Phys. Rev. B **79**, 094521 (2009).
[32] X. He, G. Li, J. Zhang, A. B. Karki, R. Jin, B. C. Sales, A. S. Sefat, M. A. McGuire, D. Mandrus, and E. W. Plummer, Phys. Rev. B **83**, 220502 (2011).
[33] J.-X. Yin, Z. Wu, J.-H. Wang, Z.-Y. Ye, J. Gong, X.-Y. Hou, L. Shan, A. Li, X.-J. Liang, X.-X. Wu, J. Li, C.-S. Ting, Z.-Q. Wang, J.-P. Hu, P.-H. Hor, H. Ding, and S. H. Pan, Nat. Phys. **11**, 543 (2015).
[34] H. Miao, P. Richard, Y. Tanaka, K. Nakayama, T. Qian, K. Umezawa, T. Sato, Y.-M. Xu, Y. B. Shi, N. Xu, X.-P. Wang, P. Zhang, H.-B. Yang, Z.-J. Xu, J. S. Wen, G.-D. Gu, X. Dai, J.-P. Hu, T. Takahashi, and H. Ding, Phys. Rev. B **85**, 094506 (2012).
[35] M. Tinkham, *Introduction to Superconductivity*, Second Ed. (Dover Publications, New York, 2004).
[36] H. Kim, C. Martin, R. T. Gordon, M. A. Tanatar, J. Hu, B. Qian, Z. Q. Mao, R. Hu, C. Petrovic, N. Salovich, R. Giannetta, and R. Prozorov, Phys. Rev. B **81**, 180503 (2010).
[37] P. Löptien, L. Zhou, A. A. Khajetoorians, J. Wiebe, and R. Wiesendanger, Surf. Sci. **643**, 6 (2016).
[38] L. Shan, Y.-L. Wang, J. Gong, B. Shen, Y. Huang, H. Yang, C. Ren, and H.-H. Wen, Phys. Rev. B **83**, 060510 (2011).
[39] C. V. Parker, A. Pushp, A. N. Pasupathy, K. K. Gomes, J. Wen, Z. Xu, S. Ono, G. Gu, and A. Yazdani, Phys. Rev. Lett. **104**, 117001 (2010).
[40] A. Kamlapure, T. Das, S. C. Ganguli, J. B. Parmar, S. Bhattacharyya, and P. Raychaudhuri, Sci. Rep. **3**, 2979 (2013).
[41] K. Bouadim, Y. L. Loh, M. Randeria, and N. Trivedi, Nat. Phys. **7**, 884 (2011).
[42] V. J. Emery and S. A. Kivelson, Nature **374**, 434 (1995).
[43] N. L. Saini, Sci. Technol. Adv. Mater. **14**, 14401 (2013).
[44] T. Hanaguri, Y. Kohsaka, J. C. Davis, C. Lupien, I. Yamada, M. Azuma, M. Takano, K. Ohishi, M. Ono, and H. Takagi, Nat. Phys. **3**, 865 (2007).
[45] T.-M. Chuang, M. P. Allan, J. Lee, Y. Xie, N. Ni, S. L. Bud'ko, G. S. Boebinger, P. C. Canfield, and J. C. Davis, Science **327**, 181 (2010).
[46] E. P. Rosenthal, E. F. Andrade, C. J. Arguello, R. M. Fernandes, L. Y. Xing, X. C. Wang, C. Q. Jin, A. J. Millis, and A. N. Pasupathy, Nat. Phys. **10**, 225 (2014).
[47] S.-H. Lee, G. Xu, W. Ku, J. S. Wen, C. C. Lee, N. Katayama, Z. J. Xu, S. Ji, Z. W. Lin, G. D. Gu, H.-B. Yang, P. D. Johnson, Z.-H. Pan, T. Valla, M. Fujita, T. J. Sato, S. Chang, K. Yamada, and J. M. Tranquada, Phys. Rev. B **81**, 220502 (2010).